Cell Reports, Volume *41*

Supplemental information

Trigeminal afferents sense locomotion-related meningeal deformations

Andrew S. Blaeser, Arthur U. Sugden, Jun Zhao, Simone Carneiro-Nascimento, Frederick B. Shipley, Hanaé Carrié, Mark L. Andermann, and Dan Levy

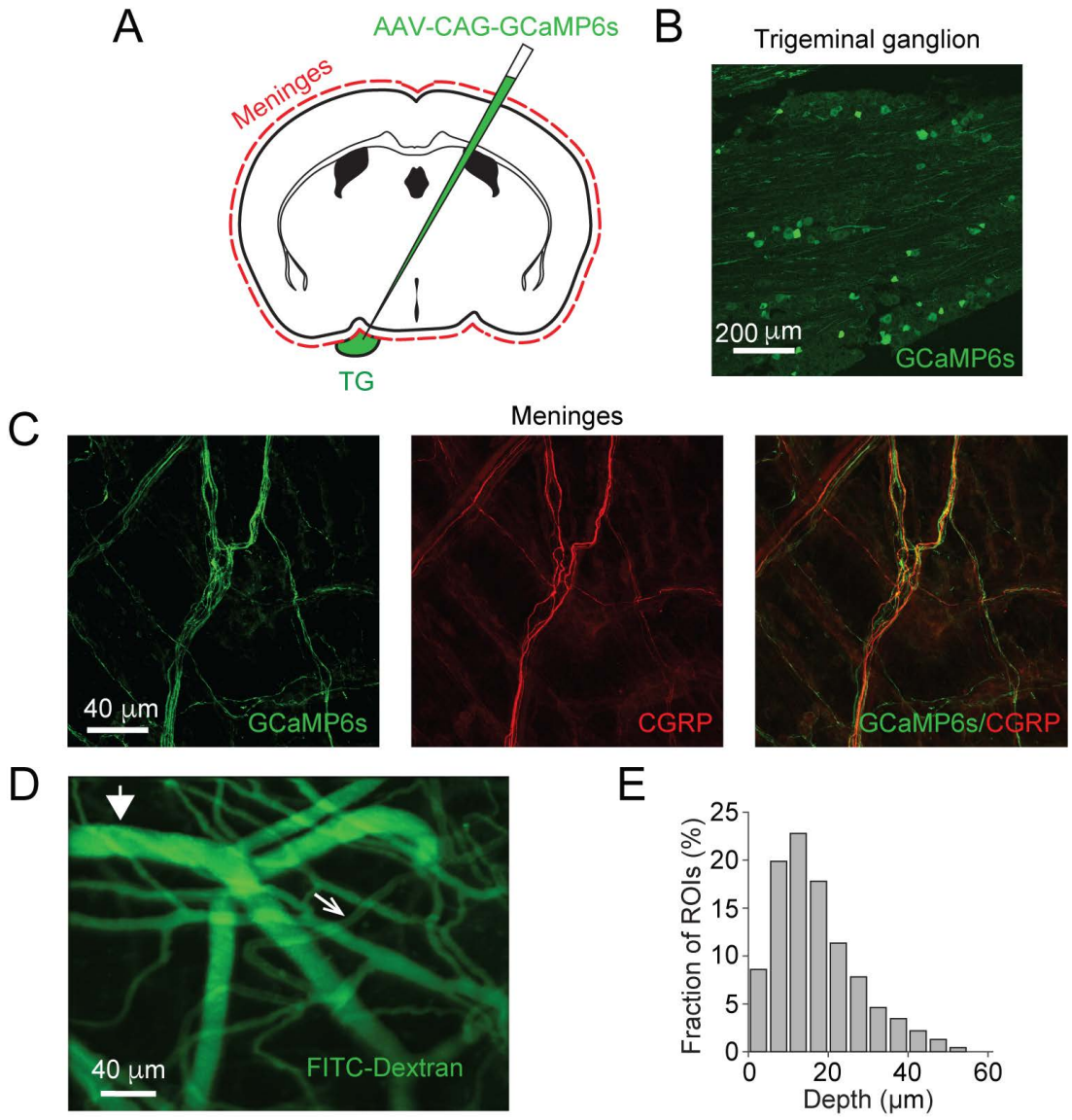

Figure S1: Anatomy of meningeal innervation. Related to Figure 1. (A) Schematic of the injection strategy for AAV-mediated expression of GCaMP6s in trigeminal ganglion neurons without damaging the ipsilateral meninges. (B) Histological section indicating GCaMP6s expression in a subset of neurons in the trigeminal ganglion. (C) Using immunohistochemistry, we identified CGRP expression in 31.7-62.2% of the dural GCaMP6s-labeled fibers (median 41.7%, 18 FOVs, n=3 mice), suggesting AAV transduction in both peptidergic and non-peptidergic meningeal afferents. (D) Maximum projection from a 15-minute volumetric imaging session of the meningeal vasculature through a cranial window implanted 2 weeks earlier. Throughout the imaging session, the vascular label (2 MDa FITC-Dextran) remained contained within both dural (thin arrow) and pial (thick arrow) blood vessels, with no detectable extravasation. (E) Histogram of ROI depth relative to the dural surface.

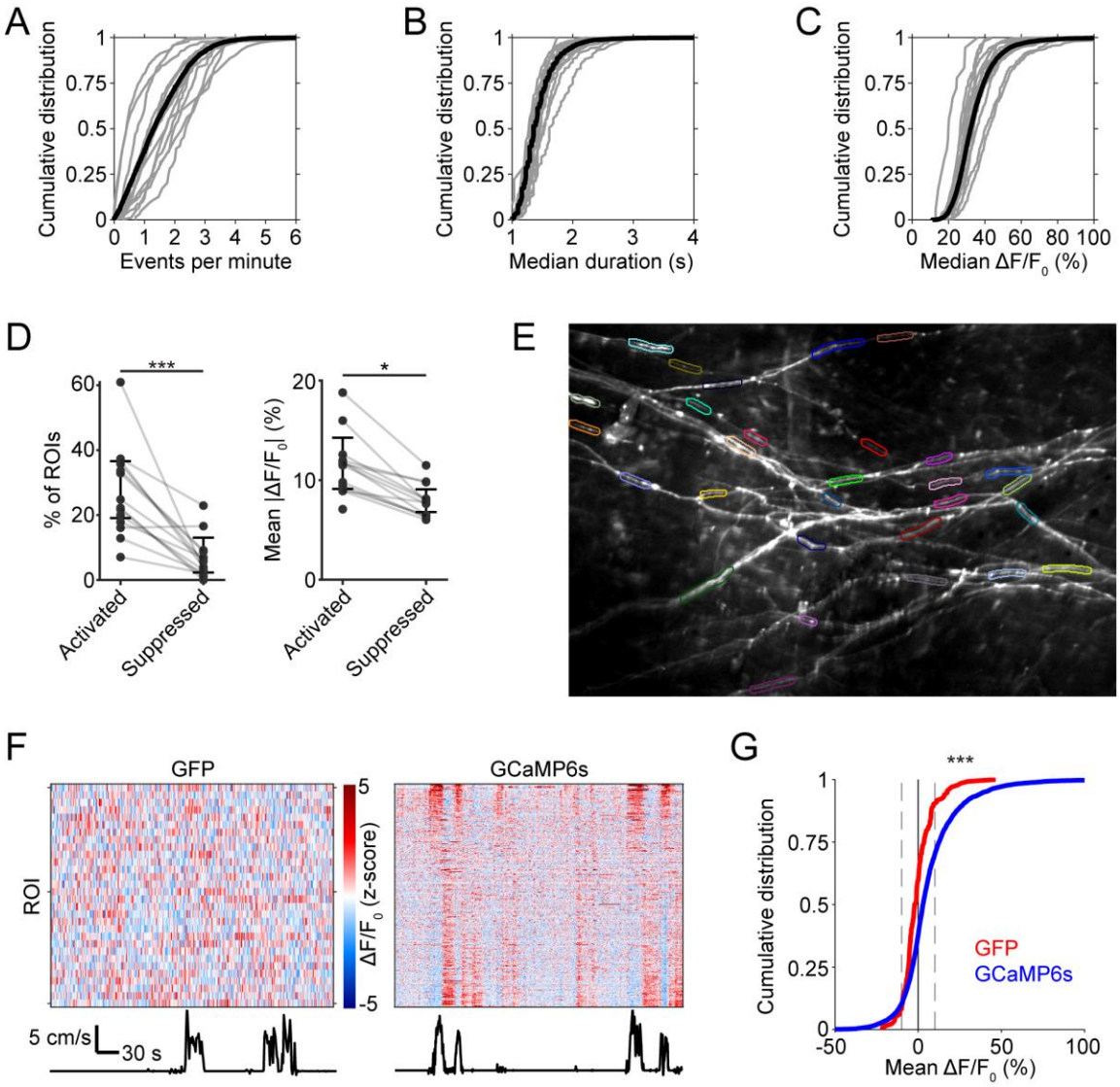

Figure S2: Characterization of spontaneous and locomotion-evoked meningeal afferent activity. Related to Figure 2. (A-C) Cumulative distribution of ROI-level event rates (A), median event durations (B), and median event amplitudes ($\Delta F/F_0$) (C), for all events observed during periods of quiet wakefulness. Gray traces represent individual FOV, and black traces represent pooling over all FOV. (D) Comparisons of the proportion (left) and mean absolute change in activity ($|\Delta F/F_0|$) (right) of all ROIs per FOV that were classified as activated or suppressed during locomotion. Error bars represent bootstrapped 95% confidence intervals of the mean. Comparison of activated vs. suppressed proportions: $p = 10^{-4}$, two-tailed iterated bootstrap. Comparison of activated vs. suppressed event magnitudes: $p = 0.016$, paired, two-tailed t-test. (E) Example mean projection of GFP-expressing meningeal afferent fibers from a FOV imaged in a control NaV1.8:Ai6 mouse. ROIs were drawn manually to resemble those obtained from the GCaMP6s data. (F) Example comparison of peri-locomotion bout fluorescence signals obtained from mice expressing GFP (left, same FOV as in E) or GCaMP6s (right) in meningeal afferents. Scale bars apply to both left and right plots. (G) Cumulative distributions of ROI-level mean locomotion-associated $\Delta F/F_0$ for GFP (red) and GCaMP6s (blue) ROIs. Dashed lines at ±5% indicate thresholds used to identify locomotion-activated or –suppressed subpopulations. $p = 1.1 \times 10^{-7}$, two-sample Kolmogorov-Smirnov test.

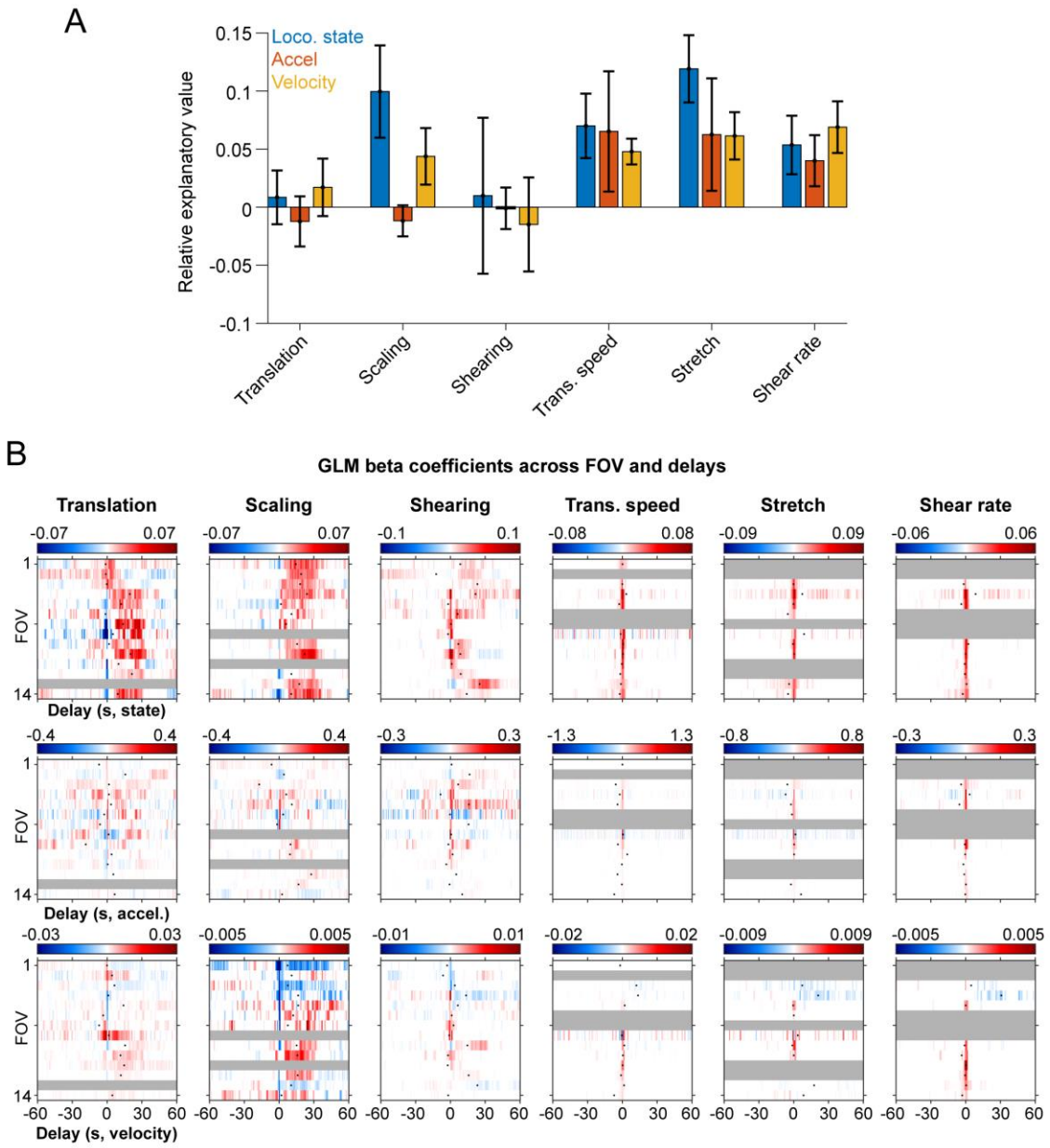

Figure S3: Modeling meningeal deformation based on locomotion parameters. Related to Figure 3. (A) Breakdown of relative explanatory value of each locomotion-related predictor to each form of deformation. Values are mean ± SEM, N = 14 FOV from 6 mice. (B) Heatmaps of GLM coefficients for each predictor (rows; top to bottom: locomotion state, acceleration, velocity) and each type of meningeal deformation (columns). Dots indicate center-of-mass estimates of typical delays between the increase in a locomotion parameter (state, acceleration, or velocity) and the consequence for each meningeal deformation type. Rows with gray shading indicate that that type of deformation was not well-fit by the GLM for the associated FOV.

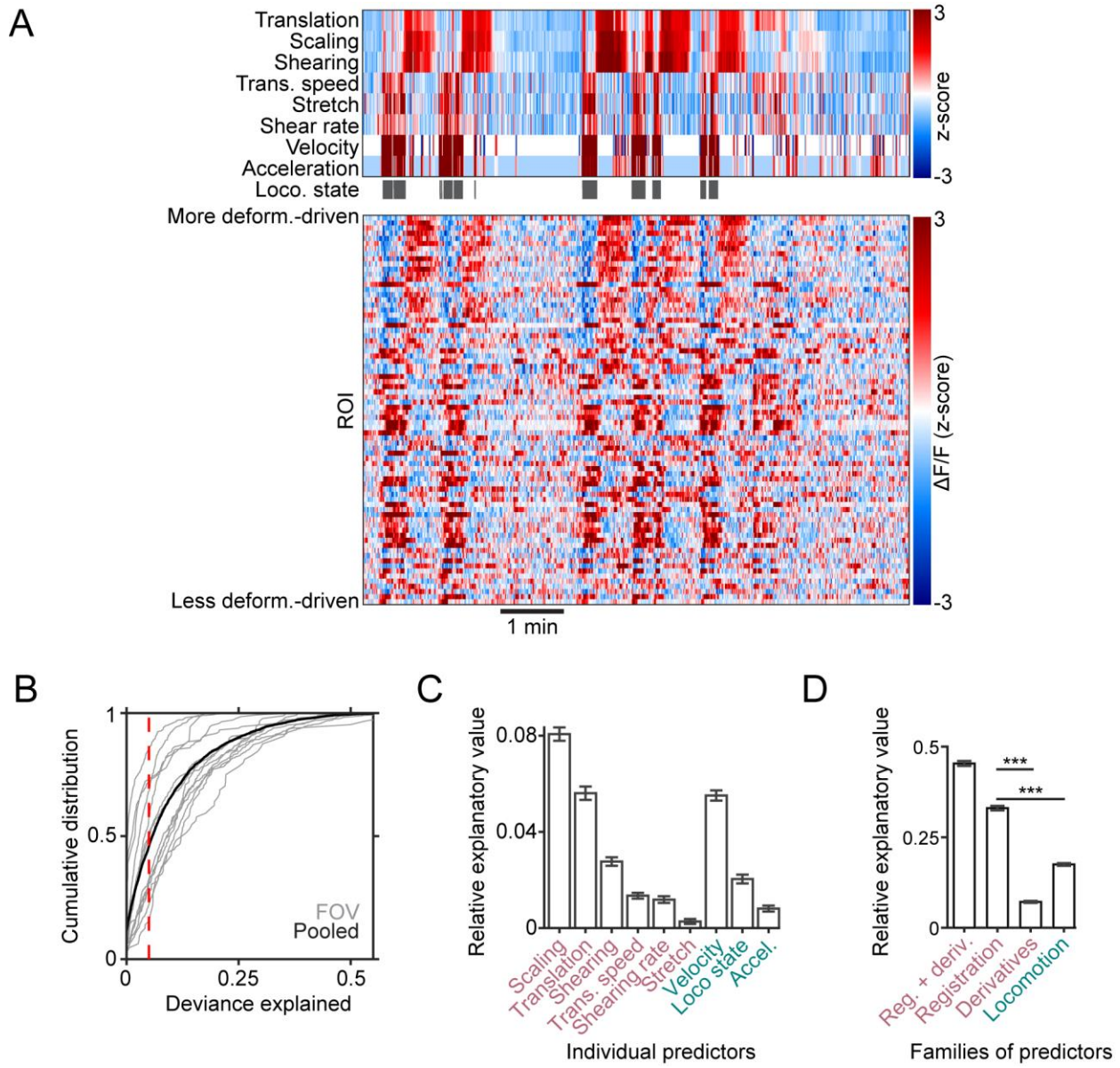

Figure S4: Modeling afferent activity from meningeal deformation and mouse locomotion. Related to Figure 4. (A) Top panel: meningeal deformation and locomotion predictor variables. Bottom: simultaneous afferent activity of putative mechanosensitive ROIs (N = 76 ROIs), sorted from most to least deformation-driven. (B) Cumulative distribution of deviance explained by the GLM for all ROIs from each experiment (gray; 14 FOVs across 6 mice) and pooled across experiments (black). (C) Relative explanatory value of each individual predictor variable for all deformation-sensitive or mixed-sensitivity afferents (mean ± SEM). (D) Breakdown of relative explanatory value of different families of predictors used to model afferent activity. Relative explanatory value was significantly different for each family: $p < 0.001$, ANOVA and post-hoc tests.

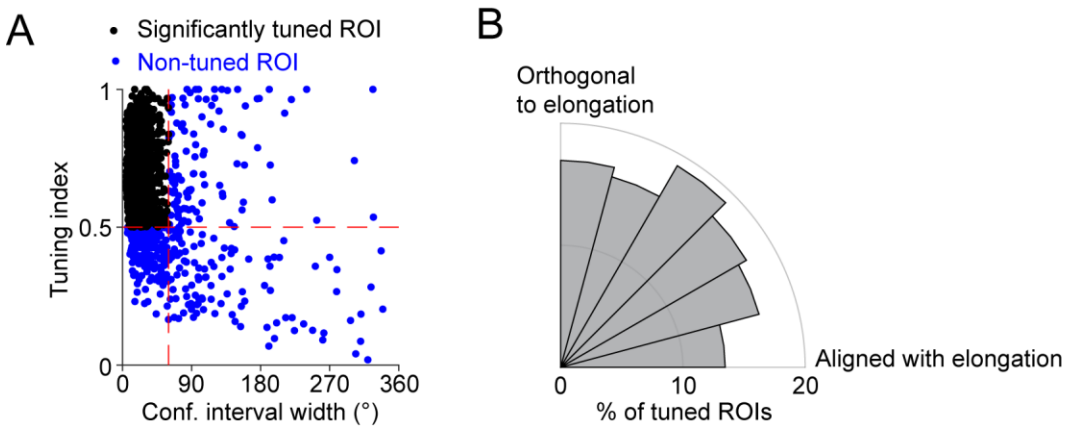

Figure S5: Characterization of tuning of meningeal afferents to angle of meningeal compression or expansion. Related to Figure 4. (A) Scatter plot of confidence interval width for each ROI's preferred tuning angle vs. angular tuning selectivity index for mechanosensitive ROIs, pooled across all FOVs. Black dots represent ROIs demonstrating significant angular tuning; blue points indicate untuned ROIs. Red dashed lines indicate cutoff values for each variable. Confidence intervals were obtained via bootstrapping. 82% of all mechanosensitive ROIs showed significant angular tuning to compression and/or expansion along specific axes. (B) Histogram of differences between each ROI's tuning angle and the axis of elongation of the ROI mask within the FOV. There was no significant relationship ($p=0.075$, bootstrapped one-way, two-tailed ANOVA, N = 1811 ROIs) between these two variables.

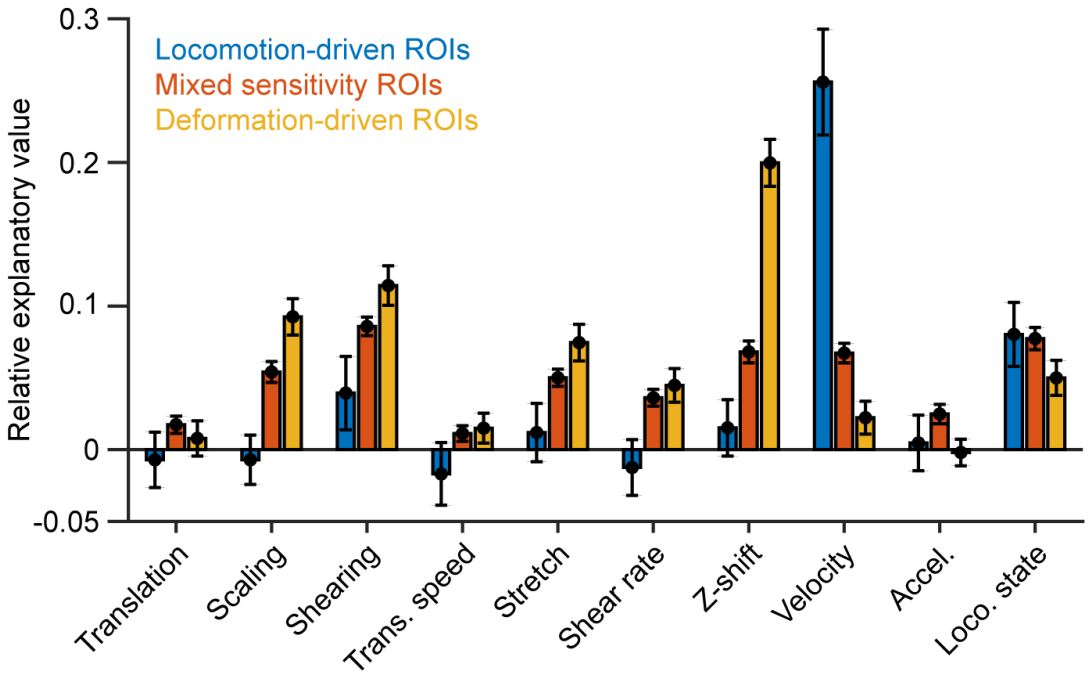

Figure S6: Modeling meningeal afferent activity from locomotion and 3D deformation. Related to Figure 5. Breakdown of the relative explanatory value of each predictor to each ROI subtype. Values are mean ± SEM. N = 61 loco. ROIs, N = 622 mixed ROIs, and N = 248 ROI deform ROIs.